Boundary-Layer Meteorology (2019) 170:45–68
https://doi.org/10.1007/s10546-018-0389-8

RESEARCH ARTICLE

Numerical Study of Turbulent Flow Fields Over Steep Terrain by Using Modified Delayed Detached-Eddy Simulations

Takeshi Ishihara[1] · **Yihong Qi**[1]

Received: 15 September 2017 / Accepted: 16 August 2018 / Published online: 6 September 2018

Abstract
Turbulent flow fields over a two-dimensional steep ridge and three-dimensional steep hill with rough and smooth surfaces are investigated by using a delayed detached-eddy simulation (DDES) with the specified height as a new control parameter. The applicability of typical turbulence models in previous studies is evaluated by using validation metrics. While all turbulence models simulate the turbulent flow fields over the steep rough terrain well, the $k-\varepsilon$ model overestimates the mean wind speed and underestimates the turbulent kinetic energy over steep, smooth terrain. The large-eddy simulation captures the large-scale vortices and improves the mean wind speed, but overestimates the turbulent kinetic energy due to the inaccurate specification of the surface roughness. The detached-eddy simulation considering the surface roughness shows further improvement, but still overestimates the turbulent kinetic energy, since the region using the Reynolds-averaged Navier–Stokes model is too thin. The modified DDES model with a new control parameter is suitable for the prediction of the mean wind speed and turbulence as demonstrated by the visualization of instantaneous flow fields through vortex cores, and a quadrant analysis to examine the organized motion, with strong organized motions identified in the wake region of smooth terrain. Roller vortices are significant on the lee side of the two-dimensional smooth ridge, while horseshoe vortices appear in the wake region of the three-dimensional smooth hill.

Keywords Delayed detached-eddy simulation · Quadrant analysis · Steep terrain · Turbulent flow fields · Validation metrics

1 Introduction

The prediction of turbulent flow over complex terrain is important for many environmental and engineering applications, such as forest-fire propagation (Kobayashi et al. 1994), forest management (Ruck and Adams 1991; Dupont et al. 2008), thermal circulations and pollutant

✉ Yihong Qi
qi@bridge.t.u-tokyo.ac.jp

Takeshi Ishihara
ishihara@bridge.t.u-tokyo.ac.jp

[1] Department of Civil Engineering, School of Engineering, The University of Tokyo, Tokyo, Japan

dispersion (Ohba et al. 2002; Fernando 2010), the safety of structures (Watanabe and Uchida 2015), and also plays a critical role in the field of wind energy. The accurate prediction of the mean flow fields is directly related to the efficient extraction of wind energy (Palma et al. 2008; Song et al. 2013), given that the wind power increases as the cube of the wind speed. Therefore, the accurate prediction of the mean wind speed is important in determining the locations where new wind turbines might be installed, such as in mountainous areas, where wind-energy resources are rich due to the speed-up caused by topography. However, as complex topography may also generate strong turbulence, which may increase the fatigue loading on wind turbines (Watanabe and Uchida 2015). The accurate prediction of turbulence is also crucial for maintaining the safety of wind turbines, particularly in complex terrain with very steep slopes, which greatly deforms the incoming turbulent flow and results in complex flows in the wake region of the terrain.

In the past few decades, numerical studies on the prediction of turbulent flows over complex terrain have been performed extensively, and are classified into three categories according to the turbulence models employed. The first category is based on Reynolds-averaged Navier–Stokes (RANS) models, which have been widely used in engineering applications. Ferreira et al. (1995) carried out a numerical study on two-dimensional ridges by using a modified low-Reynolds-number $k-\varepsilon$ model to qualitatively investigate the flow patterns in the wake of two-dimensional smooth ridges with $Re = 8 \times 10^4$ and different steepnesses. While the size of the recirculation regions were overestimated, the drag coefficients were well predicted in the case of a two-dimensional rough ridge of $Re = 1.6 \times 10^5$. Ishihara and Hibi (2002) compared the performance of the standard $k-\varepsilon$ model and Shih's non-linear $k-\varepsilon$ model (see Shih et al., 1995) on the prediction of turbulent wake flows of a three-dimensional rough hill, finding that the non-linear $k-\varepsilon$ model provides a better prediction than the standard $k-\varepsilon$ model and shows good agreement with the experimental data. Balogh et al. (2012) proposed a $k-\varepsilon$ model with an enhanced wall function for a steep, three-dimensional smooth hill and an actual hill, but the predicted turbulent kinetic energy was inadequate, and the hit rate was 50%. Blocken et al. (2015) used a revised $k-\varepsilon$ model to predict the mean wind speeds over real complex terrain consisting of an irregular succession of hills and valleys, demonstrating a predicted mean wind-speed ratio and wind direction with discrepancies of 10–20% compared with the measurements. Therefore, while it is concluded that the RANS model is able to predict turbulent flow fields well over steep terrain with rough surfaces, the model fails in cases with smooth surfaces.

The second and widely-used category is based on large-eddy simulations (LES) (Iizuka and Kondo 2004, 2006; Tamura et al. 2007; Dupont et al. 2008; Liu et al. 2016a, b). Iizuka and Kondo (2004) investigated the performance of four different subgrid-scale (SGS) models on the prediction of turbulent flow fields over two-dimensional steep ridges with two different surface roughnesses, compared their results with Ishihara et al. (2001), and found that the hybrid SGS model shows good agreement with experimental data for a two-dimensional rough ridge, but does not predict the turbulent flow well in the wake region of a two-dimensional smooth ridge. Tamura et al. (2007) studied the effect of surface roughness and curvature of two-dimensional ridges by using both the dynamic Smagorinsky and mixed models together with the immersed boundary technique to model the surface roughness, concluding that both dynamic models show good agreement with experimental data for the ridges with a gentle slope, but not for the turbulence statistics in the separated region of a steep, smooth ridge. Liu et al. (2016a) carried out numerical studies on a two-dimensional smooth ridge and a three-dimensional smooth hill, and found that the non-isotropic characteristics of turbulence in the wake region are well predicted by the LES model. However, one major issue with the LES model is the representation of surface roughness, which is

necessary in turbulent flows over real complex terrain. While the canopy model proposed by Enoki et al. (2009) has been used for surfaces covered by forests (Liu et al. 2016b), this model requires very fine grids for surfaces covered by grasses, making it expensive for engineering applications.

The third category of turbulence model combines the RANS and LES models, because the former is suitable for simulating the surface layer, and the latter is suitable for capturing vortices on the lee side of steep terrain. Such models include the detached-eddy simulation (DES) proposed by Shur et al. (1999), and a reformulation of the DES method to preserve the RANS model throughout the boundary layer proposed by Spalart et al. (2006), which is known as the delayed detached-eddy simulation (DDES). For a review of hybrid RANS/LES models, such as the DES and DDES models, see Fröhlich and Terzi (2008), where these models are mainly used in aircraft engineering and mechanical engineering in uniform flow or with a thin boundary layer. However, Bechmann and Sørensen (2010) combined a $k-\varepsilon$ model with an LES model to investigate the turbulent flow over Askervein hill, showing the model is able to capture the high turbulence level, but underestimates the mean wind speed. As mentioned by Spalart et al. (2006), the DES model exhibits an incorrect behaviour in thick boundary layers. In addition, the DDES model has not yet been applied to turbulent flows over complex terrain in thick boundary layers, making further study necessary before the reliable application of various hybrid RANS/LES models is possible over such terrain.

Section 2 describes the numerical methods, including the governing equations, turbulence models, boundary conditions and solution schemes, as well as the validation metrics and analysis methods used in the discussion. Section 3 discusses the effect of steep terrain with rough and smooth surfaces in order to quantitatively evaluate the applicability of different turbulence models based on the validation metrics. Instantaneous flow fields from the modified DDES model are then visualized by vortex cores, and examined via a quadrant analysis to investigate the organized motions in the wake region of steep terrain. Finally, conclusions are given in Sect. 4.

2 Numerical Methods

Here, the governing equations are given in Sect. 2.1, the turbulence models are described in Sect. 2.2, Sect. 2.3 presents the boundary conditions and numerical schemes, and the validation metrics and analysis methods are defined in Sect. 2.4.

2.1 Governing Equations

The finite volume method is applied for the discretization of the governing partial differential equations. The continuity and momentum equations for incompressible flow are given by, respectively,

$$\frac{\partial \rho \bar{u}_i}{\partial x_i} = 0, \tag{1}$$

$$\frac{\partial (\rho \bar{u}_i)}{\partial t} + \frac{\partial \left(\rho \bar{u}_j \bar{u}_i\right)}{\partial x_j} = -\frac{\partial \bar{p}}{\partial x_i} + \frac{\partial}{\partial x_j}\left[\mu\left(\frac{\partial \bar{u}_i}{\partial x_j} + \frac{\partial \bar{u}_j}{\partial x_i}\right)\right] + \frac{\partial \tau_{ij}}{\partial x_j} + f_{\bar{u},i}, \tag{2}$$

where $\bar{u}_i$ is the resolved velocity component in the ith direction, $\bar{p}$ is the resolved pressure, ρ is the density of the fluid, μ is the molecular viscosity, the source term $f_{\bar{u},i}$ is the fluid

force per unit grid volume, τ_{ij} is the SGS stress and is introduced to consider the difference between $\overline{u_i u_j}$ and $\bar{u}_i \bar{u}_j$,

$$\tau_{ij} = -\rho\left(\overline{u_i u_j} - \bar{u}_i \bar{u}_j\right), \tag{3}$$

where $\overline{u_i u_j}$ represents the total Reynolds stress in the computational cell.

2.2 Turbulence Models

In order to close the governing equations, the stress τ_{ij} is normally modelled using an eddy-viscosity hypothesis, where τ_{ij} is assumed as products of the fluid strain and eddy viscosity,

$$\tau_{ij} = 2\mu_t \bar{S}_{ij} + \frac{\delta_{ij}}{3}\tau_{kk}, \tag{4a}$$

$$\bar{S}_{ij} = \frac{1}{2}\left(\frac{\partial \bar{u}_i}{\partial x_j} + \frac{\partial \bar{u}_j}{\partial x_i}\right), \tag{4b}$$

respectively, where $\bar{S}_{ij}$ is the strain-rate tensor, and μ_t is the eddy viscosity. In the DDES model,

$$\mu_t = \rho C_\mu \frac{\bar{k}^2}{\bar{\varepsilon}}, \tag{5}$$

where $C_\mu = 0.09$ (Fluent Theory Guide 2012), and $\bar{k}$ and $\bar{\varepsilon}$ are the turbulent kinetic energy (TKE) and the dissipation rate of TKE, respectively. The term $\left(\delta_{ij}/3\right)\tau_{kk}$ is absorbed into the pressure term (Bechmann and Sørensen 2010), while $\bar{k}$ and $\bar{\varepsilon}$ are obtained by solving

$$\frac{\partial\left(\rho\bar{k}\right)}{\partial t} + \frac{\partial\left(\rho\bar{k}\bar{u}_i\right)}{\partial x_i} = \frac{\partial}{\partial x_j}\left[\left(\mu + \frac{\mu_t}{\sigma_k}\right)\frac{\partial \bar{k}}{\partial x_j}\right] + G_k + Y_k, \tag{6}$$

$$\frac{\partial(\rho\bar{\varepsilon})}{\partial t} + \frac{\partial(\rho\bar{\varepsilon}\bar{u}_i)}{\partial x_i} = \frac{\partial}{\partial x_j}\left[\left(\mu + \frac{\mu_t}{\sigma_\varepsilon}\right)\frac{\partial \bar{\varepsilon}}{\partial x_j}\right] + C_{1\varepsilon}G_k\frac{\bar{\varepsilon}}{\bar{k}} - C_{2\varepsilon}\rho\frac{\bar{\varepsilon}^2}{\bar{k}}, \tag{7}$$

respectively, with

$$G_k = \mu_t\left|\bar{S}\right|^2, \tag{8a}$$

$$\left|\bar{S}\right| = \sqrt{2\bar{S}_{ij}\bar{S}_{ij}}, \tag{8b}$$

$$Y_k = -\rho\bar{k}^{3/2}/l. \tag{9}$$

Here, G_k represents the generation of TKE due to the mean velocity gradients, and is parametrized in Eq. 8 in a manner consistent with the Boussinesq hypothesis. The term Y_k represents the dissipation of TKE, the values of the constants are $C_{1\varepsilon} = 1.44$, $C_{2\varepsilon} = 1.92$, $\sigma_k = 1$ and $\sigma_\varepsilon = 1.3$ (Fluent Theory Guide 2012), and l is the turbulence length scale. In the DDES model (Fluent Theory Guide 2012),

$$l = l_{RANS} - f_d \max(0, l_{RANS} - l_{LES}), \tag{10}$$

where l_{RANS} and l_{LES} are the turbulence length scales of the RANS and LES models, respectively, f_d is a control function to select the regions applying the RANS and LES models, and l_{RANS}, l_{LES} and f_d are written as, respectively,

$$l_{RANS} = \bar{k}^{3/2}/\bar{\varepsilon}, \tag{11}$$

$$l_{LES} = C_{des}\Delta_{max}, \tag{12}$$

$$f_d = 1 - \tanh\left[(A_1\gamma_d)^{A_2}\right], \quad A_1 = \begin{cases} 20 & d < h_s \\ 0.2 & d \geq h_s \end{cases}, \tag{13}$$

where the constant $C_{des} = 0.032$ suggested by Oka and Ishihara (2009) is adopted, and $\Delta_{max} = \max(\Delta x, \Delta y, \Delta z)$ is used as described in the Fluent Theory Guide (2012). The parameter γ_d is calculated as

$$\gamma_d = \frac{\upsilon_t + \upsilon}{\kappa^2 d^2 \sqrt{U_{ij}U_{ij}}}, \tag{14a}$$

$$U_{ij} = \frac{\partial \bar{u}_i}{\partial x_j}, \tag{14b}$$

where υ_t is the kinematic eddy viscosity, υ is the molecular viscosity, $\kappa = 0.41$ is the von Kármán constant, d is the distance to the closest wall, h_s is the specified height described below, and U_{ij} is the velocity gradient.

In the Fluent Theory Guide (2012), $A_1 = 20$ (proposed by Gritskevich et al. 2012) and $A_2 = 3$ are used for the realizable $k - \varepsilon$ model and the shear-stress transport, $k - \varepsilon$ based DDES models, while $A_1 = 8$ (proposed by Spalart et al. 2006) and $A_2 = 3$ are used for the Spalart–Allmaras-based DDES model. However, the constants of A_1 specified in Gritskevich et al. (2012) and Spalart et al. (2006) are optimized to simulate the flow fields around an obstacle with a thin boundary layer and have not been validated for simulation of the flow over a ridge or a hill immersed in a thick boundary layer, such as the atmospheric boundary layer. Here, a piecewise function of A_1 is proposed to limit the application of the RANS model in the region below the specified height h_s, where $A_1 = 0.2$ is recommended when the distance to the closest wall $d > h_s$, and the default value of $A_1 = 20$ is retained if the distance $d < h_s$. The definition of h_s and the optimization process for A_1 are explained below.

The experimental scale of 1/1000, as shown in Ishihara et al. (1999), means the specified height $h_s = 1$ mm in the simulation for the wind-tunnel case corresponds to a value of 1 m at full scale. This specified height does not change with the boundary-layer height or the hill height, and can be used for all full-scale cases. It is also used to determine whether the logarithmic law or the canopy model should be selected as a surface-roughness model for simulations of engineering flows of thick boundary layers. Vegetation and obstacles higher than 1 m in the real scale are recommended to be modelled by the canopy model.

In order to optimize the value of A_1 for the flow simulations in a thick boundary layer, the value of A_1 is varied from 20 to 0.1, with Fig. 1 showing the corresponding variation of the value of f_d in the vertical direction at $x/h = 3.75$ and $y/h = 0$ on the lee side of the three-dimensional smooth hill. Here, as $f_d = 0$ implies the use of the realizable $k - \varepsilon$ model, while $f_d = 1$ represents the use of the LES model, the parameter f_d limits the height of the interface of the realizable $k - \varepsilon$ and LES models. The height of the interface is about $51h_s$ when $A_1 = 20$ is adopted, which implies that the realizable $k - \varepsilon$ model is used to simulate the turbulent flow below 51 mm, which exceeds the hill height of $40h_s$ used here, with the LES model only used above this height. The height of the interface decreases as the value of A_1 decreases, and is approximately h_s when $A_1 = 0.2$ is used. However, $f_d \neq 0$ below h_s when $A_1 < 0.2$ is used for the whole layer, which indicates that the realizable $k - \varepsilon$ model is not used to simulate the turbulent flow below h_s in this case. In contrast, when the proposed model for the parameter f_d (cf. Eq. 13) is used, the interface height $\approx h_s$, and the value of f_d is zero below h_s. This implies that the realizable $k - \varepsilon$ model is used to simulate the turbulent flow below a height of h_s, and the LES model is adopted above.

The predicted and measured longitudinal velocity component and TKE over a three-dimensional smooth hill in the central plane of the terrain are shown in Fig. 2 to assess the

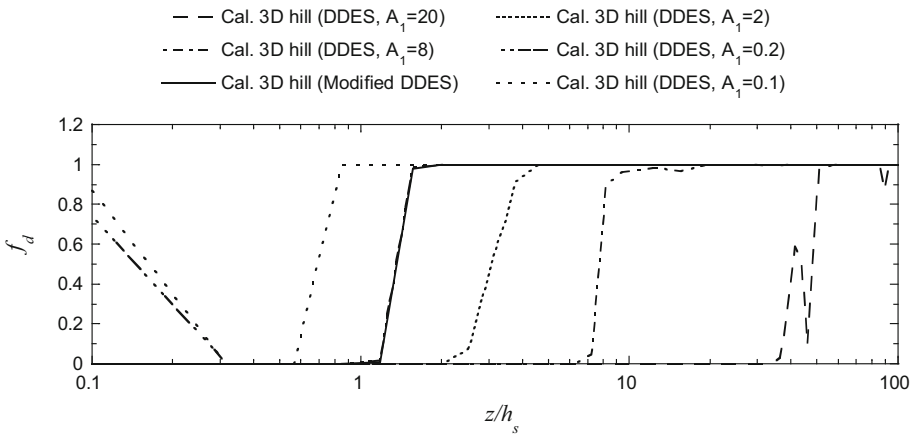

Fig. 1 Variation of the value of f_d with A_1 values in the vertical direction at $x/h = 3.75$ and $y/h = 0$ on the lee side of a three-dimensional smooth hill

performance of the parameter A_1. As expected, the predicted longitudinal velocity component and TKE by the DDES model with $A_1 = 20$ are the same as those simulated by the realizable $k - \varepsilon$ model because the region applying the RANS model is about 51 mm higher than the hill with height of $40h_s$. The predicted longitudinal velocity component is still overestimated, and the TKE is significantly underestimated. Changing $A_1 = 20$ to $A_1 = 8$, as originally proposed by Spalart et al. (2006), or even to $A_1 = 2$, does not improve the accuracy, with the TKE still underestimated. While the predicted longitudinal velocity component and TKE are improved when A_1 is dramatically reduced to $A_1 = 0.2$, they still do not approach those values observed in the wind tunnel test, since the realizable $k - \varepsilon$ model is not used to simulate the turbulent flow below h_s in these cases. The predicted longitudinal velocity component and TKE show good agreement with those from the wind tunnel test when the proposed Eq. 13 is used.

As discussed above, when $A_1 < 0.2$, the model parameter is not sensitive for $d > h_s$, because $f_d = 1$ above h_s, as shown in Fig. 1. Therefore, $A_1 = 0.2$ is selected as an optimal value above h_s, since the height of the interface is about h_s as expected when $A_1 = 0.2$ is adopted. The DDES model with the optimal value is hereafter the modified DDES model. The applicability of this model for different terrain and surface roughness is discussed in Sect. 3 in detail.

Table 1 summarizes the turbulence viscosity and length scale of the typical turbulence models, with the turbulence models differing only in the way they calculate the turbulence viscosity and length scale. The modified DDES model uses a mixed turbulence length scale and has the same turbulence length scale as the DES model for $f_d = 1$. The DES model simply selects the smaller turbulence length scale obtained from the RANS and LES models. The turbulence length scale l_{RANS} is implicitly calculated using the variables $\bar{k}$ and $\bar{\varepsilon}$, while the turbulence length scale l_{LES} is explicitly calculated based on the local grid size. In general, the value of l_{RANS} is smaller than the value of l_{LES} near the ground and, thus, the RANS model is selected there, while the value of l_{LES} is smaller in the region away from the ground when the LES model is used.

Here, the two-equation turbulence model is used in the modified DDES, DES and $k - \varepsilon$ models to calculate the turbulence viscosity, while a zero-equation turbulence model, namely the Smagorinsky model (1963), is used in the LES model to estimate the turbulence viscosity. These models are shown in Table 1, where the variable L_s is the mixing length at the SGS, κ

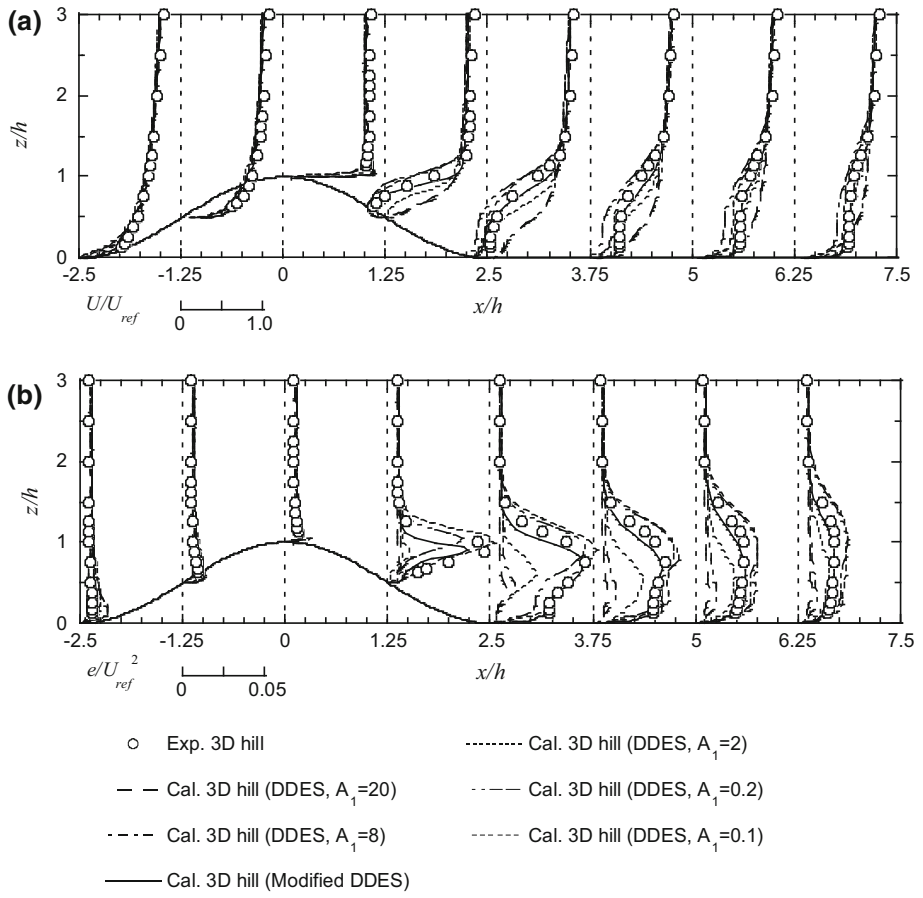

Fig. 2 Predicted and measured **a** longitudinal velocity component U, and **b** TKE e over a three-dimensional smooth hill in the central plane of the terrain

$= 0.41$ is the von Kármán constant, and d is the distance to the closest wall. The parameter C_s is the Smagorinsky constant, and is set to 0.032 as shown by Oka and Ishihara (2009). The parameter Δ is the local grid size, and is computed according to the cell volume by using $\Delta = V^{1/3}$. Detailed derivations and calculations can be found in the Fluent Theory Guide (2012).

2.3 Boundary Conditions and Numerical Scheme

The inlet boundary condition in the modified DDES model, as well as in the LES and DES models, is a uniform flow, and the turbulent inflow is generated by the blocks used in the wind-tunnel experiments conducted by Ishihara et al. (1999, 2001). On the other hand, the measured mean wind speed and TKE are directly used as the inlet boundary conditions for the $k - \varepsilon$ model. The pressure outlet is used for the outlet boundary, and the symmetry condition is adopted for the side and upper boundaries, which are the same as those used in other turbulence models.

Table 1 Summary of the turbulence viscosity and turbulence length scale

Turbulence model	Turbulence viscosity, μ_t	Turbulence length scale, l
DDES model	$\mu_t = \rho C_\mu \frac{\bar{k}^2}{\bar{\varepsilon}}$	$l = l_{RANS} - f_d \max(0, l_{RANS} - l_{LES})$
DES model	$\mu_t = \rho C_\mu \frac{\bar{k}^2}{\bar{\varepsilon}}$	$l = \min(l_{RANS}, l_{LES})$
$k-\varepsilon$ model	$\mu_t = \rho C_\mu \frac{\bar{k}^2}{\bar{\varepsilon}}$	$l = \frac{\bar{k}^{\frac{3}{2}}}{\bar{\varepsilon}}$
LES model	$\mu_t = \rho l_s^2 \lvert\bar{S}\rvert$	$l_s = \min(\kappa d, C_s \Delta)$

The rough surface is expressed by the canopy model proposed by Enoki et al. (2009). The equivalent drag coefficient, packing density, representative length scale, and the height of the canopy layer are $C_f = 0.2$, $\gamma_0 = 0.6\%$, $l_0 = 0.01$ mm, and $H_c = 5$ mm, respectively. As explained in Sect. 3.1, the scale ratio of the experimental terrain is 1/1000, thus the canopy parameters correspond to a forest at full scale of height $H_c = 5$ m, and leaf-area density $\gamma_0/l_0 = 0.6$ m^{-1}. The drag coefficient $C_f = 0.2$ is the same as the value used by Dupont et al. (2008) for a forest of height $H_c = 10$ m at full scale. The leaf-area density $\gamma_0/l_0 = 0.6$ m^{-1} is higher than the value of $\gamma_0/l_0 = 0.16$ m^{-1} used by Dupont et al. (2008), since the density of the model tree in the wind tunnel test is much higher than that in the full-scale forest.

For the wall-adjacent cells, the wall shear stresses are obtained from the laminar stress–strain relationship in the laminar sublayer,

$$\frac{\bar{u}}{u_*} = \frac{\rho u_* z}{\mu}. \tag{15}$$

If the mesh cannot resolve the laminar sublayer, the centroid of the wall-adjacent cells is assumed to fall within the logarithmic region of the boundary layer, and then the law of the wall is employed,

$$\frac{\bar{u}}{u_*} = \frac{1}{\kappa} \ln\left(E \frac{\rho u_* z}{\mu}\right) - \Delta B, \tag{16}$$

where $\bar{u}$ is the resolved wind speed in the direction tangential to the wall, z is the distance between the centre of the cell and the wall, u_* is the friction velocity, and the constant $E = 9.793$. Here, the parameter ΔB accounts for the displacement caused by the rough wall, and is zero for the smooth wall used in the LES model.

The logarithmic law as shown in Eq. 17 is also widely used as the boundary condition for the neutrally-stratified atmospheric boundary layer (see Grimmond and Oke 1999; Xue et al. 2002; Blocken et al. 2007),

$$\frac{\bar{u}}{u_*} = \frac{1}{\kappa} \ln\left(\frac{z}{z_0}\right), \tag{17}$$

where z_0 is the aerodynamic roughness length. The relationship between the parameters ΔB and z_0 can be derived by comparing Eqs. 16 and 17, and expressed as

$$\Delta B = \frac{1}{\kappa} \ln\left(E \frac{\rho u_* z_0}{\mu}\right). \tag{18}$$

A finite volume method and an unstructured collocated mesh are used for the present simulations. A second-order, central-difference scheme is used for the convective and viscosity terms, and a second-order implicit scheme for the unsteady term. The Semi-Implicit

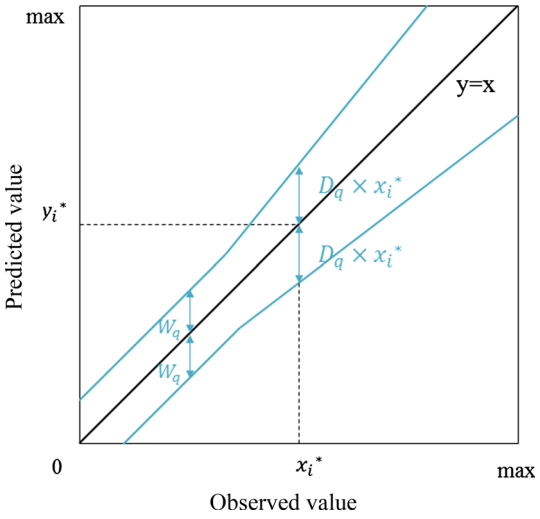

Fig. 3 Illustration of the validation metrics employed here. The blue lines represent the boundaries of the accurate region for q and the black line for $\boldsymbol{y} = \boldsymbol{x}$

Pressure Linked Equations (SIMPLE) algorithm (Ferziger and Peric, 2002) is employed for solving the discretized equations. These numerical schemes are used for both the modified DDES model and for the other turbulence models, with only the $k - \varepsilon$ model adopting the Quadratic Upstream Interpolation for Convective Kinematics (QUICK) scheme for the spatial discretization.

2.4 Validation Metrics and Analysis Methods

In order to quantify the agreement between the computational and experimental results, the hit rate q is used as a validation metric (see Schatzmann et al. 2010 and Oettl 2015), and is defined as

$$q = \frac{1}{N}\sum_{i=1}^{N} n_i, \text{ with } \quad n_i = \begin{cases} 1 & \left|\frac{y_i - x_i}{x_i}\right| \leq D_q \quad \text{or} \quad |y_i - x_i| \leq W_q \\ 0 & \text{else} \end{cases}, \tag{19}$$

where x_i and y_i are the observed (measured) and predicted (computed) values of a given variable for sample i, respectively, and N is the number of data points. The boundaries of the accurate region are shown schematically in Fig. 3, with blue lines for q, and the black line for $y = x$. The values of metrics corresponding to perfect agreement and disagreement are $q = 1$ and $q = 0$, respectively. Following the German VDI guideline 3783-9 (VDI, 2005), the thresholds $D_q = 0.25$ and $W_q = 0.07 \sim 0.1|\text{max}|$ are used, as suggested by Schatzmann et al. (2010) and Oettl (2015). The thresholds for q are $D_q = 0.15$ for the mean wind speed, and $D_q = 0.3$ for the TKE, since the squared variable gives errors twice the values of the variable itself. Another threshold $W_q = 0.05|\text{max}|$ is used for both the mean wind speed and TKE in which |max| is a maximum value in the observation and the prediction, as shown in Fig. 3.

Vorticity is a dynamic quantity usually used to identify vortices, though, as mentioned by Kida and Miura (1998), vorticity alone cannot distinguish between swirling and shearing motions. Instead, the λ_2-criterion proposed by Jeong and Hussain (1995) is used, which

searches for a local pressure minimum due to vortical motions, defining a vortex core as a connected region with two negative eigenvalues of the system,

$$\bar{S}_{ik}\bar{S}_{kj} + \bar{\Omega}_{ik}\bar{\Omega}_{kj} = 0, \tag{20}$$

$$\bar{\Omega}_{ij} = \frac{1}{2}\left(\frac{\partial \bar{u}_i}{\partial x_j} - \frac{\partial \bar{u}_j}{\partial x_i}\right), \tag{21}$$

where $\bar{S}_{ij}$ is the rate-of-strain tensor defined in Eq. 4b, and $\bar{\Omega}_{ij}$ is the vorticity tensor. This definition equals the requirement that the eigenvalue for the second mode λ_2 is negative when three eigenvalues are ordered as $\lambda_1 \leq \lambda_2 \leq \lambda_3$.

A quadrant analysis is also used for the quantitative evaluation of organized motions (see Rajagopalan and Antonia 1982; Oikawa and Meng 1995), with the four quadrants of the Reynolds stress defined as

$$S_n(uw) = \begin{cases} -\overline{uw} & \text{for} \quad (u > 0, w > 0) \text{ if} \quad n = 1 \\ -\overline{uw} & \text{for} \quad (u < 0, w > 0) \text{ if} \quad n = 2 \\ -\overline{uw} & \text{for} \quad (u < 0, w < 0) \text{ if} \quad n = 3 \\ -\overline{uw} & \text{for} \quad (u > 0, w < 0) \text{ if} \quad n = 4, \end{cases} \tag{22}$$

where u and w are the instantaneous velocity components in the longitudinal and vertical directions. The quadrants $S_2(uw)$ and $S_4(uw)$ represent ejection and sweep motions, respectively, and make positive contributions to the Reynolds stress, while the quadrants $S_1(uw)$ and $S_3(uw)$ express outward and inward motions, respectively, and make negative contributions to the Reynolds stress. The difference ΔS between the values of S_4 and S_2 is a measure of the intensity of the organized motions. When the turbulent flow is fully developed and evolves randomly, the value of ΔS is close to zero, but non-zero when organized motions are present. Here, the organized motions include large-scale vortex shedding, as well as the coherent motion immersed in a nominal random process.

3 Numerical Results and Discussion

In this section, two steep terrains with two different surface conditions are discussed. The numerical configuration is first described in Sect. 3.1. The turbulent flow fields over two-dimensional ridges and three-dimensional hills with smooth and rough surfaces are then investigated by the modified DDES model in Sects. 3.2, 3.3 and the applicability of typical turbulence models is evaluated in terms of the validation metrics in Sect. 3.3. Finally, instantaneous flow fields over steep terrain are visualized through vortex cores, and organized motions are examined by a quadrant analysis in Sect. 3.4.

3.1 Numerical Configuration

This study focuses on the neutrally stratified boundary layer. As proxies for real atmospheric boundary-layer flows, wind-tunnel experiments are used to provide detailed data for the validation of turbulence models. The experimental data over steep, two-dimensional ridges and three-dimensional hills with smooth and rough surfaces based on the experiments carried out by Ishihara et al. (1999, 2001) are selected to evaluate the performance of the modified DDES model and the typical turbulence models. These experiments were conducted in a closed return wind tunnel with a test section 1.1 m wide, 0.9 m high, and 7 m long. Three types of cubic roughness blocks with heights of 60, 20, and 10 mm, were located at the

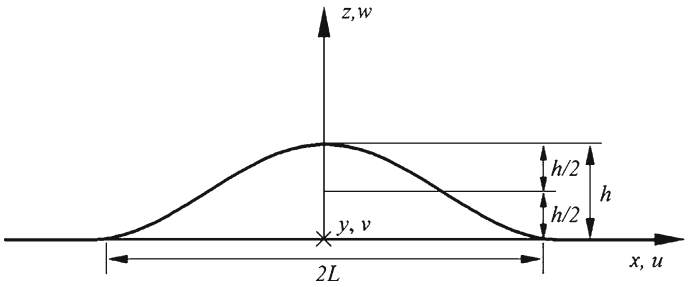

Fig. 4 Cross-section of steep ridges and hills

beginning of the test section to generate a neutrally-stratified atmospheric boundary layer. Two types of surface roughness were considered. The smooth surface represents a ground covered by grasses at full scale, and the rough surface implies a ground covered by forests with a height of 5 m at full scale. The model hills with a scale ratio of 1/1000 have a cosine-squared cross-section as shown in Fig. 4, and are expressed as

$$z_s = \begin{cases} h\cos^2\left(\pi \frac{r}{2L}\right) & r < L \\ 0 & r \geq L. \end{cases} \tag{23}$$

The hill height is $h = 40$ mm and the base radius is $L = 100$ mm, and thus the maximum slope is approximately 32°; $r = \sqrt{x^2 + y^2}$ and $r = x$ are used for three-dimensional hills and two-dimensional ridges, respectively.

The computational domain for the simulations with the modified DDES model shown in Fig. 5a has a width of 0.66 m and an additional upstream zone of 2 m prior to the roughness blocks to avoid perturbations from the inlet boundary. The centre of the steep hill is located 3.4 m downstream of the roughness blocks used in the experiment. The nested grid system is adopted in the horizontal plane to resolve small vortices in the wake region of steep terrain. In the fine-grid region, the grid dependence was systematically tested by changing the horizontal grid resolution from 1 mm to 10 mm, with a horizontal resolution of 2 mm found to be fine enough here. In the vertical direction, the minimum grid resolution is 0.2 mm, with 4 and 11 grid layers within the recommended specified height and canopy layer, respectively. The σ grid system is applied to modify the vertical coordinate of grid nodes above the steep terrain. Figures 5b, c show the grid distribution on the ground in the simulations with the LES, DES, and modified DDES models. In the simulations with the $k - \varepsilon$ model, the calculation domain and grid system are used as shown by Ishihara and Hibi (2002). The size of the computational domain is $L_x \times L_y \times L_z = 2.4\text{m} \times 0.8\text{m} \times 0.9\text{m}$.

Table 2 summarizes the terrain types and aerodynamic parameters used in the numerical simulations. Here, Re_h is the global Reynolds number, U_h is the wind speed at the height of $z/h = 1$ for flat terrain. The rough case is imitated by a canopy layer of 5-mm height located on the surface of roughness $z_0 = 0.01$ mm, and the smooth case is simulated by only using $z_0 = 0.01$ mm.

3.2 Turbulent Flow Fields Over Steep Terrain with Rough Surface

Shown in Fig. 6 are profiles of longitudinal and vertical velocity components normalized by U_{ref}, which is the mean wind speed over the flat terrain with a rough surface at $x/h = 0$ and $z/h = 2$, over the two-dimensional ridge and the three-dimensional hill with a rough surface

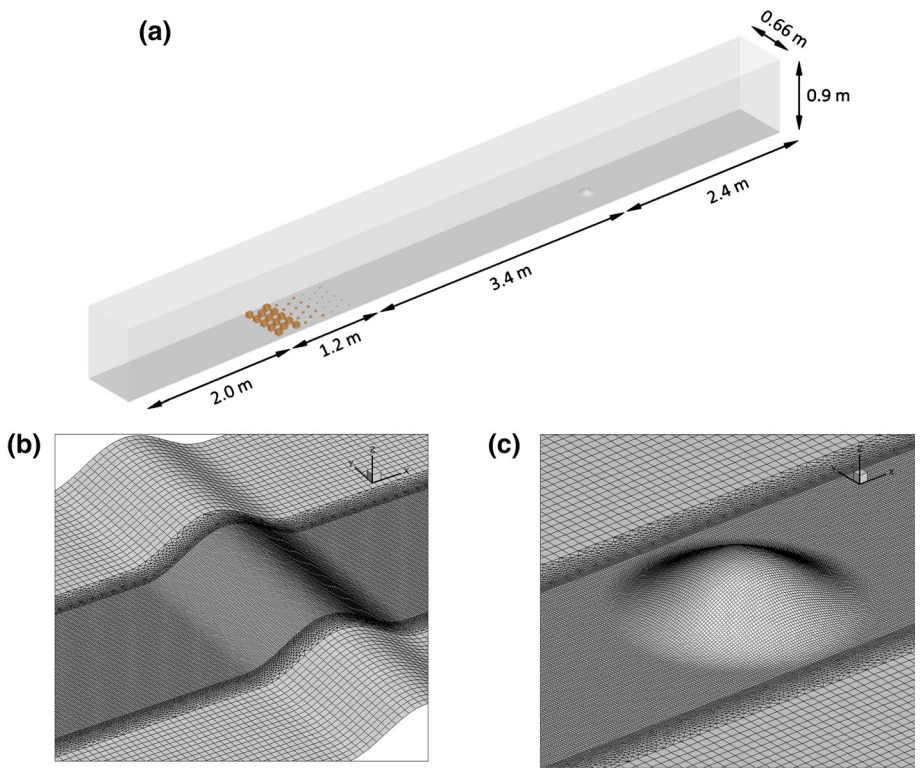

Fig. 5 Computational domain **a** and grid distribution on the ground of the **b** two-dimensional ridge and **c** three-dimensional hill

Table 2 Aerodynamic parameters in the numerical simulations (scale of 1/1000) over the terrain types corresponding to a two-dimensional ridge and a three-dimensional hill

Case	Terrain type	Surface	z_0 (mm)	Canopy height (mm)	$Re_h = U_h h/\nu$
1	Ridge	Rough	0.01	5	1.0×10^{-4}
2	Hill	Rough	0.01	5	1.0×10^{-4}
3	Ridge	Smooth	0.01	0	1.2×10^{-4}
4	Hill	Smooth	0.01	0	1.2×10^{-4}

in the central plane of the terrain. The bold line in black describes the shape of the terrain and the line in green indicates the upper boundary of the canopy layer. The dashed lines mark the measurement positions in the longitudinal direction.

For the two-dimensional rough ridge and the three-dimensional rough hill, the longitudinal and vertical velocity components are well predicted by the modified DDES model. The longitudinal velocity components show an obvious acceleration at the crest of terrain. The height of the speed-up region increases as the downstream distance increases and the maximum height reaches about $z/h = 2$. The longitudinal velocity components are the same for the two-dimensional ridge and the three-dimensional hill on the upstream side and in the wake region close to the terrain. However, the difference increases as the downstream

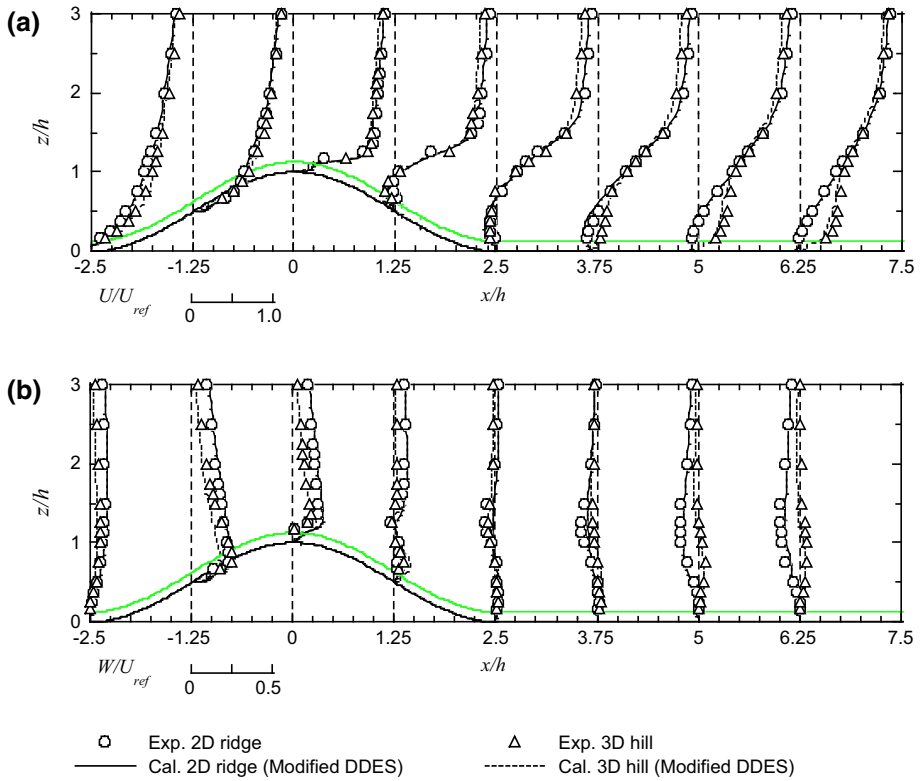

Fig. 6 Predicted and measured **a** longitudinal and **b** vertical velocity components over the two-dimensional rough ridge and the three-dimensional rough hill in the central plane of the terrain

distance increases and is limited in the region below $z/h = 1$. The faster recovery of the longitudinal velocity component in the wake region of the three-dimensional hill, compared with that in the wake region of the two-dimensional ridge, is attributed to the transportation and mixing of flows from the sides of the three-dimensional hill. The updraft flows are clearly observed on the upwind side of the crest. In the wake region, the vertical velocity components become negative in the rear of terrain element. The vertical velocity components over the two-dimensional ridge are larger than those over the three-dimensional hill, which indicates that the ridge provides a stronger blockage effect than the hill.

Figure 7 shows profiles of the square roots of the three normal stress components normalized by U_{ref} over the two-dimensional ridge and the three-dimensional hill with a rough surface in the central plane of the terrain, illustrating that the predicted three normal stress components by the modified DDES model show better agreement with the experimental results. Larger stress values are observed in the wake region of the two-dimensional rough ridge and the three-dimensional rough hill, resulting from flow separation on the lee slope of the two-dimensional ridge and the three-dimensional hill. Similar to the longitudinal velocity component, the clear difference between the longitudinal normal stress over the two-dimensional ridge and the three-dimensional hill is observed in the wake region, with the difference increasing as the downstream distance increases, and limited in the region

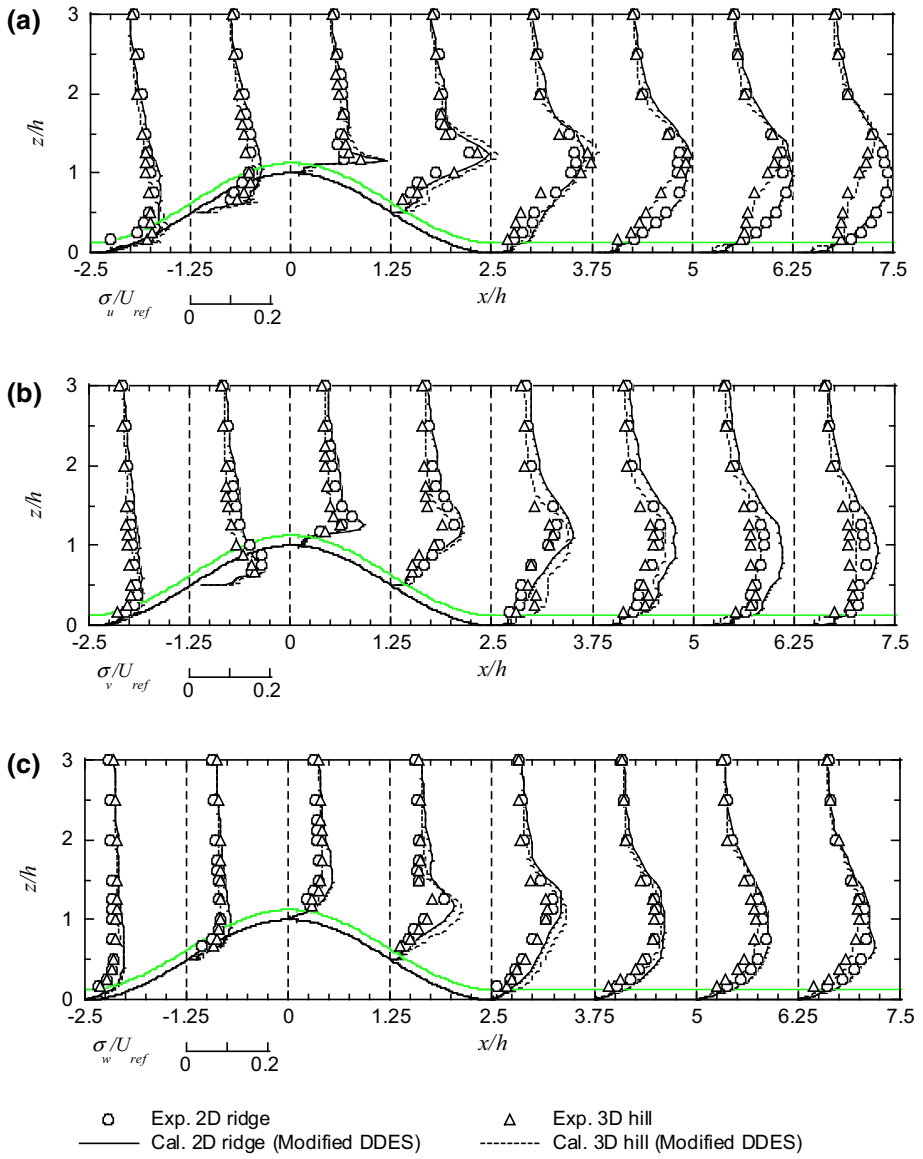

Fig. 7 Predicted and measured **a** longitudinal, **b** lateral and **c** vertical normal stress components over the two-dimensional rough ridge and the three-dimensional rough hill in the central plane of terrain

$z/h < 1.5$. However, the differences between the lateral and vertical normal stresses over the two-dimensional ridge and the three-dimensional hill are small.

The longitudinal velocity component and TKE on the lee side of the two-dimensional rough ridge and the three-dimensional rough hill at $x/h = 3.75$ and $y/h = 0$ are shown in Fig. 8. Steady and unsteady simulations by the $k - \varepsilon$ model are carried out to investigate the performance of the unsteady RANS model. All turbulence models show good agreement with experimental data for both the longitudinal velocity component and the TKE.

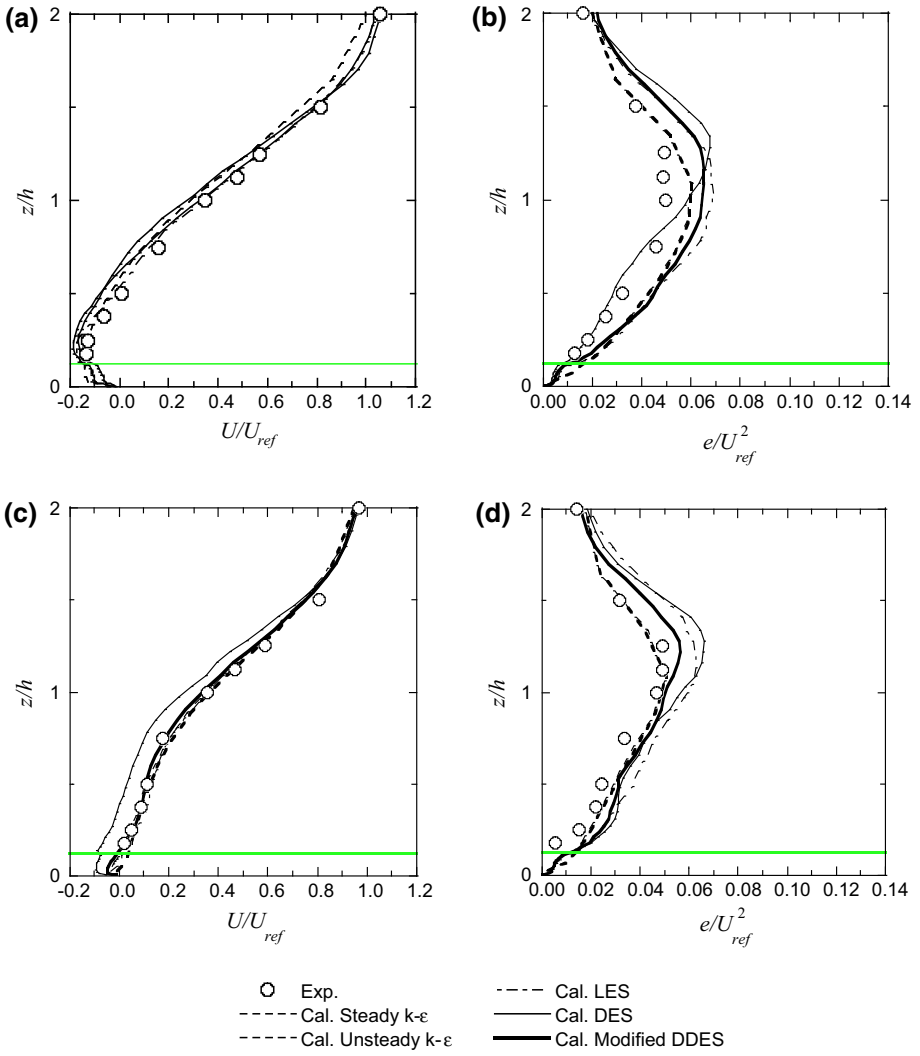

Fig. 8 Predicted and measured mean wind speed and TKE e by several turbulence models: **a** longitudinal velocity component and **b** TKE at the location $x/h = 3.75$ and $y/h = 0$ on the lee side of the two-dimensional rough ridge, **c** longitudinal velocity component and **d** TKE at the location $x/h = 3.75$ and $y/h = 0$ on the lee side of the three-dimensional rough hill

Comparisons between numerical results and experimental data over the two-dimensional rough ridge and the three-dimensional rough hill at the measurement positions are shown in Fig. 9, with blue lines indicating the boundaries defined by the value of the hit rate q, illustrating that most points for both models are located within the boundaries, independent of the turbulence model. The validation metrics for all turbulence models are summarized in Table 3, indicating reasonable accuracy for the predictions of the turbulent flow fields over the steep terrain with a rough surface.

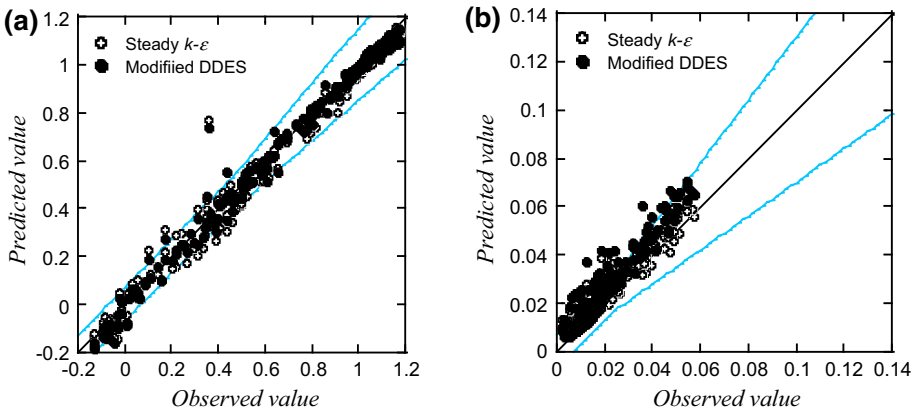

Fig. 9 Comparison between numerical results and experimental data over the two-dimensional rough ridge and the three-dimensional rough hill: **a** normalized longitudinal velocity component $\boldsymbol{U/U_{ref}}$, **b** normalized TKE $\boldsymbol{e/U_{ref}^2}$

Table 3 Validation metrics for the cases of the two-dimensional ridge and three-dimensional hill with rough and smooth surfaces

Turbulence model	Rough ridge and hill		Smooth ridge and hill	
	U/U_{ref}	e/U_{ref}^2	U/U_{ref}	e/U_{ref}^2
Steady $k-\varepsilon$ model	0.90	0.77	0.73	0.62
Unsteady $k-\varepsilon$ model	0.89	0.78	0.73	0.63
LES	0.96	0.73	0.80	0.63
DES	0.81	0.75	0.96	0.72
Modified DDES	0.93	0.77	0.95	0.95

3.3 Turbulent Flow Fields Over Steep Terrain with Smooth Surface

Profiles of the longitudinal and vertical velocity components over the two-dimensional ridge and the three-dimensional hill with a smooth surface in the central plane of the terrain are shown in Fig. 10, illustrating that the longitudinal and vertical velocity components for the two-dimensional ridge and the three-dimensional hill with a smooth surface are also well predicted by the modified DDES model. The longitudinal velocity components over the two-dimensional smooth ridge and the three-dimensional smooth hill accelerate and reach their maximum values at the crest, where the longitudinal velocity component is almost constant below $z/h=3$. The longitudinal velocity component is more pronounced in the wake region of the steep terrain with a smooth surface than that of the steep terrain with a rough surface. Furthermore, the height of the speed-up region is about $z/h=1.5$, which is slightly lower than that in the rough cases. Similar to the rough case, the difference between the longitudinal velocity components over the two-dimensional smooth ridge and the three-dimensional smooth hill in the wake region increases as the downstream distance increases. However, this difference reaches a maximum at the region close to the ground since the surface roughness is small. Profiles of normalized vertical velocity components over the two-

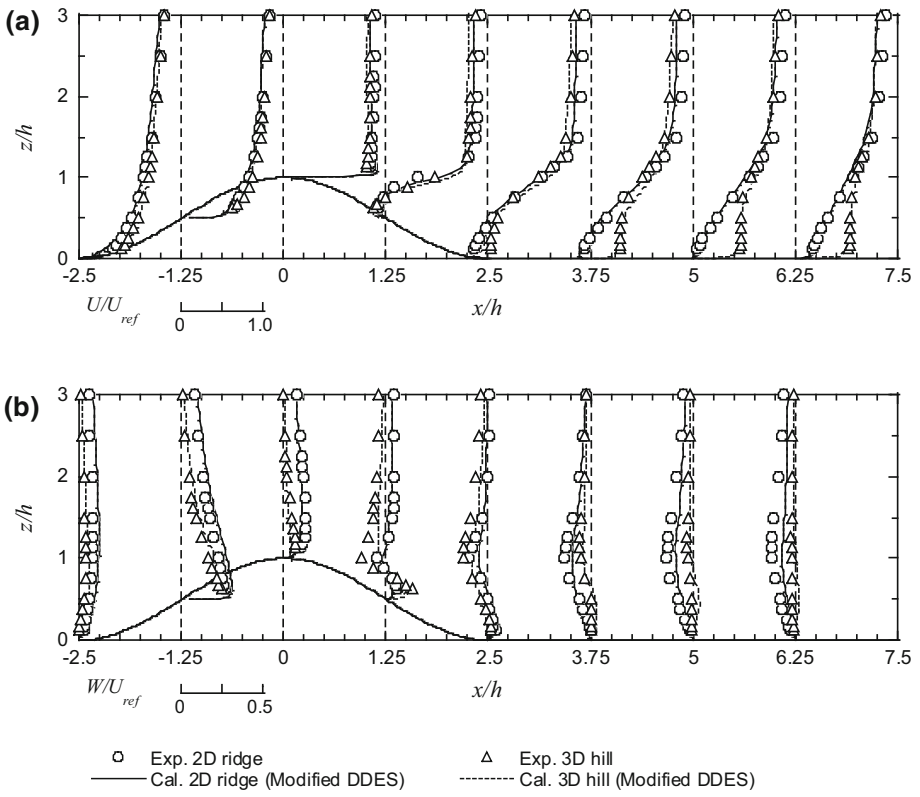

Fig. 10 Predicted and measured **a** longitudinal and **b** vertical components over the two-dimensional smooth ridge and the three-dimensional smooth hill in the central plane of the terrain

dimensional smooth ridge and the three-dimensional smooth hill are shown in Fig. 10b, which shows similar characteristics to those in the rough cases with relatively larger magnitudes.

Vertical profiles of the square roots of the three normal stress components over the two-dimensional smooth ridge and the three-dimensional smooth hill in the central plane of the terrain are shown in Fig. 11, illustrating the predicted normal stress components by the modified DDES model to be in good agreement with the experimental data. The lateral normal stresses show secondary local maxima in the so-called wall layer, which could not be observed in the rough case. In this layer, the longitudinal normal stresses show a roughly constant value. It should be noted that, for the rough case, the secondary peaks in the lateral normal stress profiles are weak, indicating that increases in surface roughness reduce turbulent motions in the spanwise direction.

The longitudinal velocity component and TKE on the lee side of the two-dimensional smooth ridge and the three-dimensional smooth hill at $x/h = 3.75$ and $y/h = 0$ are shown in Fig. 12, illustrating that steady and unsteady simulations by the $k - \varepsilon$ model overestimate the longitudinal velocity component and underestimate the TKE. The steady and unsteady $k - \varepsilon$ models show almost the same results, but give a large difference in the wake region, indicating the unsteady $k - \varepsilon$ model cannot improve the accuracy of the predictions. The results by the LES model are also shown to evaluate the performance of model, for which the simulated longitudinal velocity components show good agreement with the experimental

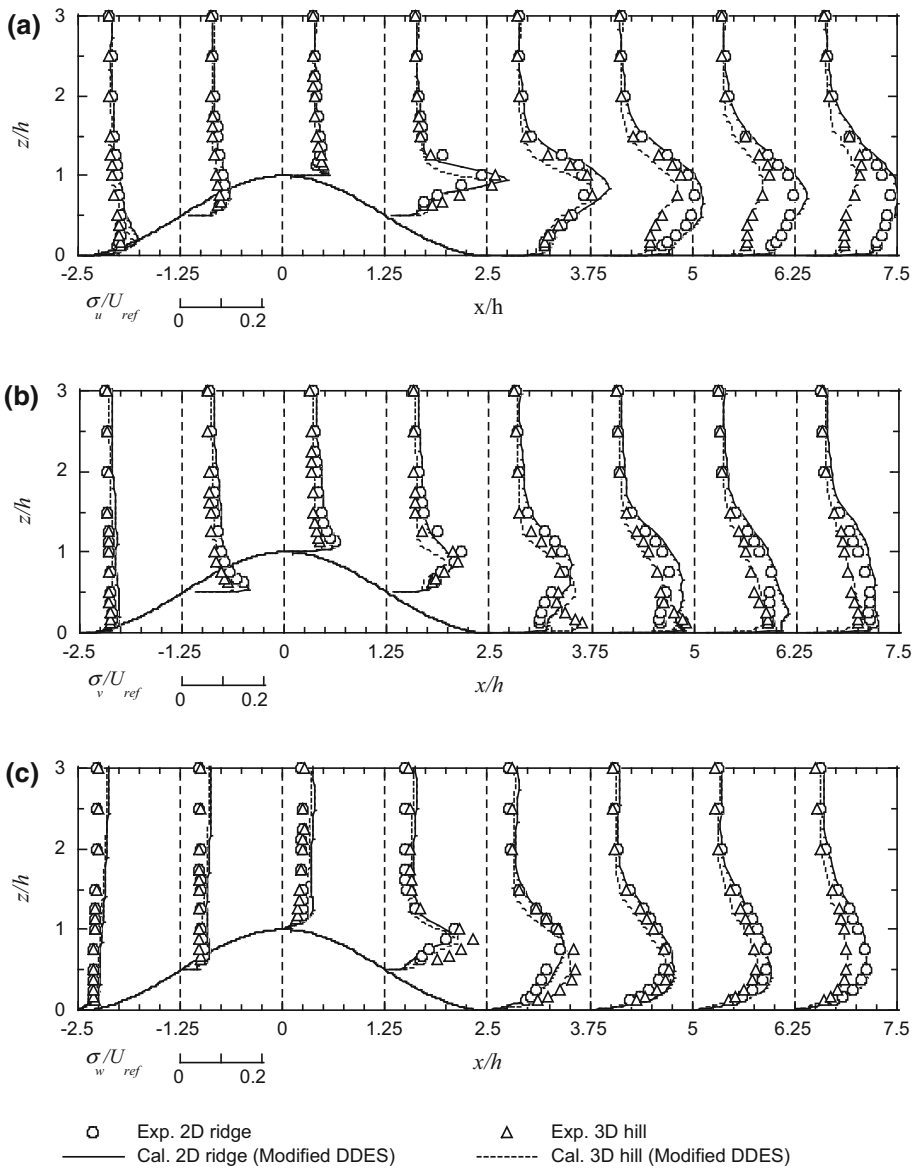

Fig. 11 Predicted and measured **a** longitudinal, **b** lateral and **c** vertical normal stress components over the two-dimensional smooth ridge and the three-dimensional smooth hill in the central plane of terrain

data, while the TKE is overestimated in the wake region due to inaccurate modelling of the surface roughness. For the case with surface roughness, the DES model shows further improvement on the predicted longitudinal velocity component, but still overestimates the TKE, which can be attributed to the fact that the region using the $k - \varepsilon$ model is too thin. The modified DDES model predicts both the longitudinal velocity component and the TKE well.

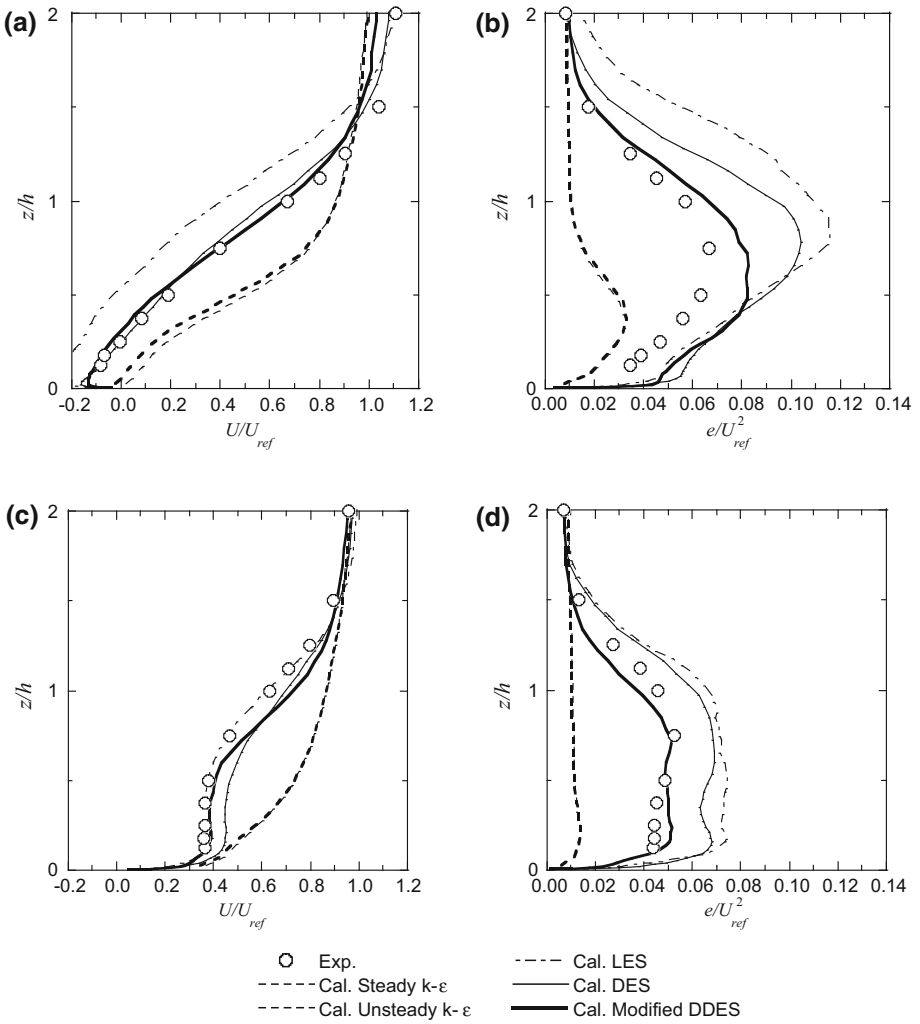

Fig. 12 Predicted and measured mean wind speed and TKE e by typical turbulence models: **a** longitudinal velocity component and **b** TKE at the location $x/h=3.75$ and $y/h=0$ on the lee side of the two-dimensional smooth ridge, **c** longitudinal velocity component and **d** TKE at the location of $x/h=3.75$ and $y/h=0$ on the lee side of the three-dimensional smooth hill

A comparison between the numerical results and experimental data over the two-dimensional smooth ridge and the three-dimensional smooth hill at the measurement positions is shown in Fig. 13, illustrating that most points of the modified DDES model are located within the boundaries defined by the value of q. However, the majority of the points of the $k-\varepsilon$ model are located above the boundaries for the wind speed and below the boundaries for the TKE, which indicates the overestimation of the mean wind speed and the underestimation of TKE by the $k-\varepsilon$ model. The validation metrics for all turbulence models are summarized in Table 3. The modified DDES model gives reasonable predictions of the turbulent flow fields over steep terrain with a smooth surface, while the $k-\varepsilon$ model shows poor accuracy for the smooth cases. As the value of q is a strict criteria, it is able to define the degree to

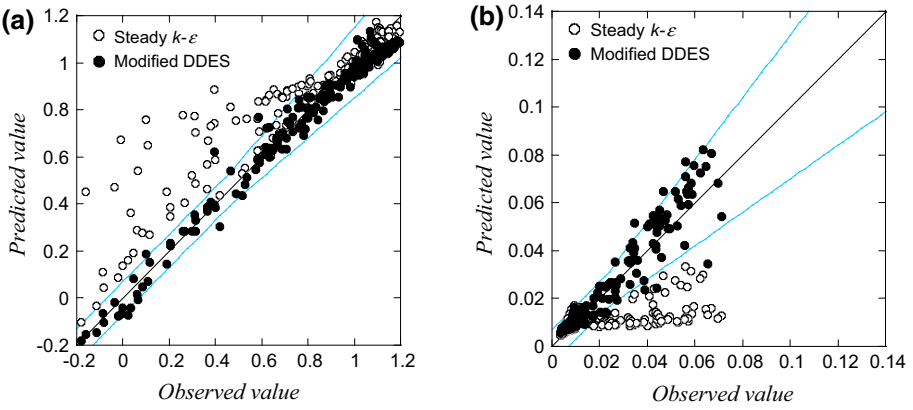

Fig. 13 Comparison between numerical results and experimental data over the two-dimensional smooth ridge and the three-dimensional smooth hill: **a** normalized longitudinal velocity component $\boldsymbol{U}/\boldsymbol{U_{ref}}$, **b** normalized TKE $\boldsymbol{e}/\boldsymbol{U_{ref}^2}$

which the modified DDES model improves the accuracy of the prediction compared with the DES and LES models.

3.4 Organized Motions in the Wake Region of Steep Terrain

To clarify the organized motions in the wake region of steep terrain, the instantaneous flow fields obtained from the modified DDES model are used to visualize the vortex cores. The iso-surface of λ_2 is used to present the vortices generated by the steep terrain, where it is found that the vortex characteristic and distribution are dominated by the surface roughness. In the rough cases, the vortices appear in the upstream region as well as in the wake region as shown in Fig. 14a, b for the two-dimensional rough ridge and in Fig. 14c, d for the three-dimensional rough hill. These vortices are enhanced by the terrain and show stochastic characteristics. In contrast, for the smooth cases, few vortices are observed in the upstream region, while the strong vortices appear in the wake region. The roller vortices on the lee side of the two-dimensional smooth ridge are clearly identified from Fig. 14e, f, and the horseshoe vortices on the lee side of the three-dimensional smooth hill are observed in Fig. 14g, h.

The difference between the vortices observed in the rough and smooth cases is quantitatively examined by using a quadrant analysis. Figure 15 shows the results of the value of ΔS from the simulations by the modified DDES model at selected locations in the longitudinal direction at an elevation of $z'/h = 1$, where $z' = z - z_s$. The values of $\Delta S(uw)$ are close to zero in the upstream region of the two-dimensional ridges and three-dimensional hills, and are independent from the surface roughness, which indicates that the organized motions in these regions are weak. The values of $\Delta S(uw)$ on the lee side of the two-dimensional rough ridge and the three-dimensional rough hill are small as shown in Fig. 15a, b, but they increase significantly on the lee side of the two-dimensional smooth ridge and the three-dimensional smooth hill as shown in Fig. 15c, d. The value of $\Delta S(uw)$ on the lee side of the two-dimensional smooth ridge is negative and shows a broad peak in the range from $x/h =$ 2.5 to $x/h = 6.5$, which is generated by the roller vortices, as shown in Fig. 14e, f, and causes strong ejection motions. The value of $\Delta S(uw)$ on the lee side of the three-dimensional smooth hill is also negative and shows a shape peak at $x/h = 2.5$, which is caused by the horseshoe

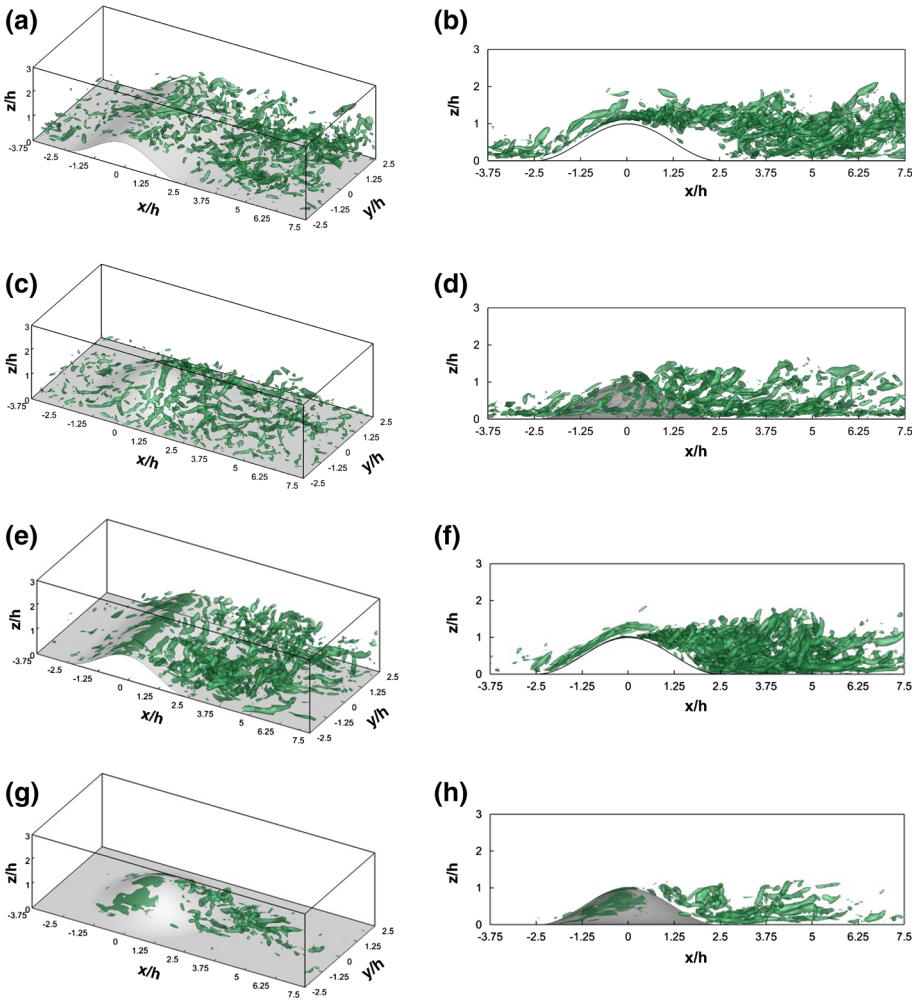

Fig. 14 Vortex cores over steep terrain with $\lambda_2 = -50{,}000$: bird's-eye view of the **a** two-dimensional rough ridge, **c** three-dimensional rough hill, **e** two-dimensional smooth ridge, **g** three-dimensional smooth hill. Side view of the **b** two-dimensional rough ridge, **d** three-dimensional rough hill, **f** two-dimensional smooth ridge, and **h** three-dimensional smooth hill

vortices, as shown in Fig. 14g, h, and generates strong ejection motions. The vortices on the lee side of the smooth terrain are organized and cannot be reproduced by the RANS models, which explains why the $k - \varepsilon$ models cannot simulate the turbulent flow well in the wake region for the smooth terrain, but give reasonable results for the rough terrain where the vortices are random and their effects are predicted by the RANS models.

4 Conclusions

Turbulent flow fields over two-dimensional steep ridges and three-dimensional steep hills with rough and smooth surfaces are investigated by numerical simulations and compared with experimental results from a wind tunnel test to yield the following conclusions.

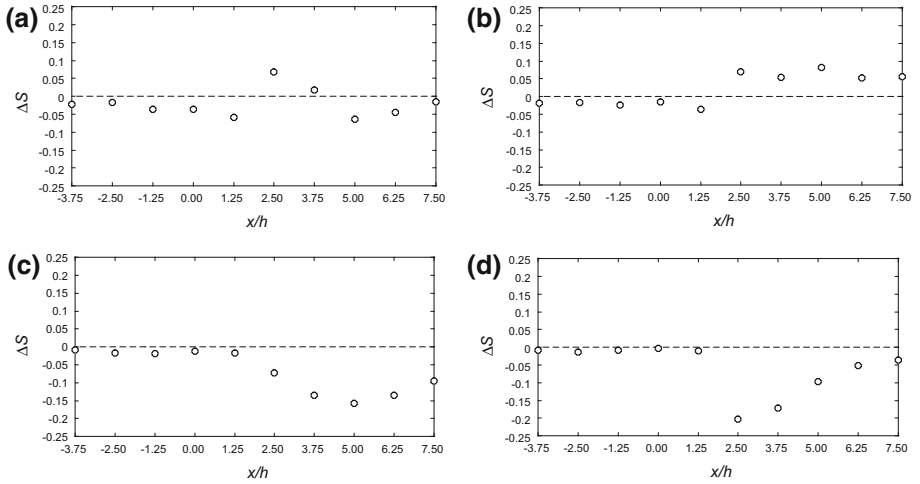

Fig. 15 Variation of the value of ΔS with the downstream distance in the central plane of steep terrain: **a** two-dimensional rough ridge at $z'/h = 1$, **b** three-dimensional rough hill at $z'/h = 1$, **c** two-dimensional smooth ridge at $z'/h = 1$, and **d** three-dimensional smooth hill at $z'/h = 1$

1. The DDES model is modified by using the specified height as a new control parameter to select the regions applying the RANS and LES models for the prediction of turbulent flow fields over steep terrain. The recommended specified height is 1 m above the ground at full scale. The predicted mean wind speed and TKE from the modified DDES model show good agreement with the experiments over steep terrain with smooth and rough surfaces.

2. All turbulence models simulate the turbulent flow fields over the steep rough terrain well. However, for the steep smooth terrain, the $k - \varepsilon$ model overestimates the mean wind speed and underestimates the TKE because the $k - \varepsilon$ model fails to reproduce organized motions in the simulation. The LES model simulates large-scale vortices and improves the mean wind speed, but overestimates the TKE due to the inaccurate representation of the surface roughness. While the DES model shows further improvement on the predicted mean wind speed, it still overestimates the TKE, since the region using the RANS model is too thin.

3. The turbulent flow fields over the steep terrain are visualized by vortex cores and are further examined by using a quadrant analysis to find that no significant organized motions are observed in the wake region of the rough terrain. However, the roller vortices are present on the lee side of the two-dimensional smooth ridge and cause ejection motions in the range from $x/h = 2.5$ to $x/h = 6.5$, while the horseshoe vortices appear on the lee side of the three-dimensional smooth hill and generate strong ejection motions at $x/h = 2.5$.

References

Balogh M, Parente A, Benocci C (2012) RANS simulation of ABL flow over complex terrain applying an enhanced $k - \varepsilon$ model and wall function formulation: implementation and comparison for Fluent and OpenFOAM. J Wind Eng Ind Aerodyn 104:360–368

Bechmann A, Sørensen NN (2010) Hybrid RANS/LES method for wind flow over complex terrain. Wind Energy 13(1):36–50
Blocken B, Stathopoulos T, Carmeliet J (2007) CFD simulation of the atmospheric boundary layer: wall function problems. Atmos Environ 41(2):238–252
Blocken B, Hout AVD, Dekker J, Weiler Q (2015) CFD simulation of wind flow over natural complex terrain: case study with validation by field measurements for Ria de Ferrol, Galicia, Spain. J Wind Eng Ind Aerodyn 147:43–57
Dupont S, Brunet Y, Finnigan JJ (2008) Large-eddy simulation of turbulent flow over a forested hill: validation and coherent structure identification. Q J R Meteorol Soc 134(636):1911–1929
Enoki K, Ishihara T, Yamaguchi A (2009) A generalized canopy model for the wind prediction in the forest and the urban area. In: Proceedings of the European Wind Energy Conference, 16–19 March 2009, Marseille, France
Fernando H (2010) Fluid dynamics of urban atmospheres in complex terrain. Annu Rev Fluid Mech 42:365–389
Ferreira AD, Lopes AMG, Viegas DX, Sousa ACM (1995) Experimental and numerical simulation of flow around two-dimensional hills. J Wind Eng Ind Aerodyn 54:173–181
Ferziger J, Peric M (2002) Computational method for fluid dynamics, 3rd edn. Springer, Berlin
Fluent Theory Guide (2012) Ansys Inc., Canonsburg, Pennsylvania
Fröhlich J, Terzi DV (2008) Hybrid LES/RANS methods for the simulation of turbulent flows. Prog Aerospace Sci 44(5):349–377
Grimmond C, Oke TR (1999) Aerodynamic properties of urban areas derived from analysis of surface form. J Appl Meteorol 38(9):1262–1292
Gritskevich MS, Garbaruk AV, Schütze J, Menter FR (2012) Development of DDES and IDDES formulations for the $k-\omega$ shear stress transport model. Flow Turbul Combust 88(3):431–449
Iizuka S, Kondo H (2004) Performance of various sub-grid scale models in large-eddy simulations of turbulent flow over complex terrain. Atmos Environ 38(40):7083–7091
Iizuka S, Kondo H (2006) Large-eddy simulations of turbulent flow over complex terrain using modified static eddy viscosity models. Atmos Environ 40(5):925–935
Ishihara T, Hibi K (2002) Numerical study of turbulent wake flow behind a three-dimensional steep hill. Wind Struct 5(2–4):317–328
Ishihara T, Hibi K, Oikawa S (1999) A wind tunnel study of turbulent flow over a three-dimensional steep hill. J Wind Eng Ind Aerodyn 83(1):95–107
Ishihara T, Fujino Y, Hibi K (2001) A wind tunnel study of separated flow over a two-dimensional ridge and a circular hill. J Wind Eng 89:573–576
Jeong J, Hussain F (1995) On the identification of a vortex. J Fluid Mech 285:69–94
Kida S, Miura H (1998) Identification and analysis of vortical structures. Eur J Mech B Fluids 17(4):471–488
Kobayashi MH, Pereira JCF, Siqueira MBB (1994) Numerical study of the turbulent flow over and in a model forest on a 2D hill. J Wind Eng Ind Aerodyn 53(3):357–374
Liu ZQ, Ishihara T, Tanaka T, He XH (2016a) LES study of turbulent flow fields over a smooth 3-D hill and a smooth 2-D ridge. J Wind Eng Ind Aerodyn 153:1–12
Liu ZQ, Ishihara T, He XH, Niu HW (2016b) LES study on the turbulent flow fields over complex terrain covered by vegetation canopy. J Wind Eng Ind Aerodyn 155:60–73
Oettl D (2015) Quality assurance of the prognostic, microscale wind-field model GRAL 14.8 using wind-tunnel data provided by the German VDI guideline 3783-9. J Wind Eng Ind Aerodyn 142:104–110
Ohba R, Hara T, Nakamura S, Ohya Y, Uchida T (2002) Gas diffusion over an isolated hill under neutral, stable and unstable conditions. Atmos Environ 3:5697–5707
Oikawa S, Meng Y (1995) Turbulence characteristics and organized motion in a suburban roughness sublayer. Boundary-Layer Meteorol 74(3):289–312
Oka S, Ishihara T (2009) Numerical study of aerodynamic characteristics of a square prism in a uniform flow. J Wind Eng Ind Aerodyn 97(11):548–559
Palma JMLM, Castro FA, Ribeiro LF, Rodrigues AH, Pinto AP (2008) Linear and nonlinear models in wind resource assessment and wind turbine micro-siting in complex terrain. J Wind Eng Ind Aerodyn 96(12):2308–2326
Rajagopalan S, Antonia RA (1982) Use of a quadrant analysis technique to identify coherent structures in a turbulent boundary layer. Phys Fluids 25:949–956
Ruck B, Adams E (1991) Fluid mechanical aspects of the pollutant transport to coniferous trees. Boundary-Layer Meteorol 56(1–2):163–195
Schatzmann M, Olesen H, Franke J (2010) COST 732 model evaluation case studies: approach and results. COST Office Brussels, 121 pp
Shih TH, Zhu J, Lumley JL (1995) A new Reynolds stress algebraic equation model. Comput Methods Appl Mech Eng 125:287–302

Shur M, Spalart P R, Strelets M, Travin A (1999) Detached-eddy simulation of an airfoil at high angle of attack. In: Proceedings of the 4th international symposium on engineering turbulence modelling and measurements, 24–26 May 1999, Ajaccio, Corscia, France

Smagorinsky J (1963) General circulation experiments with the primitive equations: I. The basic experiment. Mon Weather Rev 91(3):99–164

Song M, Chen K, He ZY, Zhang X (2013) Bionic optimization for micro-siting of wind farm on complex terrain. Renew Energy 50:551–557

Spalart PR, Deck S, Shur ML, Squires KD, Strelets MKH, Travin A (2006) A new version of detached-eddy simulation, resistant to ambiguous grid densities. Theor Comput Fluid Dyn 20(3):181–195

Tamura T, Cao S, Okuno A (2007) LES study of turbulent boundary layer over a smooth and a rough 2D hill model. Flow Turbul Combust 79(4):405–432

VDI (2005) Environmental meteorology—prognostic microscale windfield models—evaluation for flow around buildings and obstacles. Tech. Rep., VDI guideline 3783, Part 9. Beuth Verlag, Berlin

Watanabe F, Uchida T (2015) Micro-siting of wind turbine in complex terrain: simplified fatigue life prediction of main bearing in direct drive wind turbines. Wind Eng 39(4):349–368

Xue X, Wang T, Sun QW, Zhang WM (2002) Field and wind-tunnel studies of aerodynamic roughness length. Boundary-Layer Meteorol 104(1):151–163